

Computation-Guided Development of Platinum Alloy Catalyst for Carbon Monoxide Preferential Oxidation

Yanbo Pan,^{†,||} Sang Youp Hwang,^{†,||} Xiaochen Shen,[†] Jinlong Yang,^{‡,||} Jie Zeng,^{*,‡,||} Mingzai Wu,^{*,§} and Zhenmeng Peng^{*,†,||}

[†]Department of Chemical and Biomolecular Engineering, The University of Akron, Akron, Ohio 44325, United States

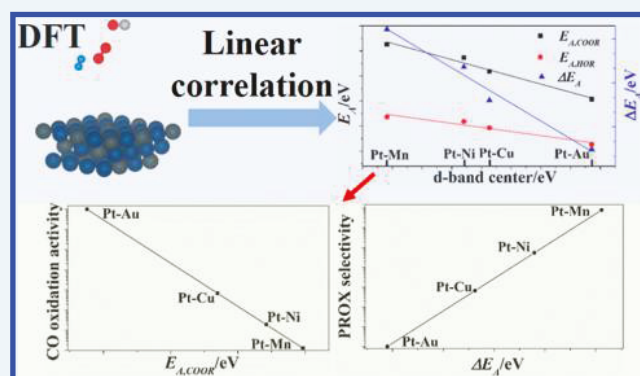
[‡]Hefei National Laboratory for Physical Sciences at the Microscale, Key Laboratory of Strongly-Coupled Quantum Matter Physics of Chinese Academy of Sciences, and Department of Chemical Physics, University of Science and Technology of China, Hefei, Anhui 230026, People's Republic of China

[§]School of Physics and Materials Science, Anhui University, Hefei, Anhui 230601, People's Republic of China

Supporting Information

ABSTRACT: Carbon monoxide preferential oxidation (PROX) in an H₂-rich stream represents one promising H₂ purification technology but requires the development of active and selective catalysts to make the technology viable. We conducted density functional theory simulations of CO PROX catalysis on model Pt alloy systems to establish correlations between the catalyst parameters and the catalytic properties, which validated $E_{A,COOR}$ and $E_{A,HOR}$ as descriptors for CO oxidation and H₂ oxidation kinetics, ΔE_A as a descriptor for CO PROX selectivity, and ϵ_d as a catalyst parameter descriptor for the activation energy barriers. We discovered an interesting compromising relationship between the CO PROX activity and selectivity properties. Pt-Ni and Pt-Mn nanoparticle catalysts were selected for synthesis on the basis of the computational data and tested for their properties, which matched well with the DFT calculations and verified the effectiveness of the computational findings. The use of computation-guided methods and the discovered catalyst parameter–property relationships would establish a rational strategy to aid catalyst development and foster CO PROX research.

KEYWORDS: computation-guided catalyst design, platinum, bimetallic catalysts, carbon monoxide, PROX



1. INTRODUCTION

CO preferential oxidation (PROX) in an H₂-rich stream has received significant research interest for supplying clean H₂ in applications such as polymer electrolyte membrane fuel cells (PEMFCs)^{1–3} and ammonia synthesis.^{4–6} For instance, PEMFCs require the use of high-purity H₂ as a fuel. To date most H₂ is produced from steam re-forming of hydrocarbons, which generates a considerable content of CO as a byproduct. While the water-gas shift reaction (WGS) can effectively convert a large part of CO to CO₂, it is only capable of decreasing the CO level to about 1% due to thermodynamic restrictions.⁷ Such a CO content is still too high and can readily deactivate Pt-based catalysts in PEMFCs. Thus, it is important to further lower the CO concentration in an H₂-rich stream to be below 10–100 ppm, a tolerable level for these catalysts.^{4,8} CO PROX offers one promising process to achieve this objective by selectively removing CO from H₂ prior to its applications.

A great number of catalyst materials have been developed and studied in CO PROX so far, with the intention of achieving a good catalyst with both high activity and selectivity in the

operating temperature range. Many transition-metal nanoparticle catalysts were found to be active for this reaction and have been intensely investigated.^{9–14} However, most of them did not fulfill both the activity and selectivity requirements. For example, highly dispersed Au nanoparticles on reducible supports can exhibit excellent activity for CO oxidation at low temperature, following the Mars–van Krevelen (MvK) mechanism.^{11,15} However, the PROX selectivity is relatively low, largely caused by the fact that H₂ oxidation could not be effectively inhibited on the catalyst surface. Pure Pt follows the Langmuir–Hinshelwood (L-H) mechanism for catalyzing CO oxidation and has little activity at low temperature. It is attributed to the strong adsorption of CO to the Pt surface, which prohibits dissociative O₂ adsorption and consequently its reaction.^{10,16} Even though O₂ can become adsorbed to allow effective CO oxidation at an elevated temperature, H₂ would

Received: January 12, 2018

Revised: May 14, 2018

Published: May 16, 2018

also react with adsorbed oxygen at this temperature and cause a low selectivity.¹⁷

Recent studies with Pt alloy (Pt-M) nanoparticle catalysts reported the improved activity and selectivity properties in comparison to their pure metal counterparts,^{18–21} and this approach has attracted considerable attention over the past few years. The tunability of Pt-M chemical composition and nanostructure provides a great number of opportunities for the development of highly active and selective CO PROX catalysts by controlling the size, morphology, and structure parameters of the bimetallic nanoparticles.²² For instance, YSZ (yttria-stabilized zirconia)-supported Pt-Co catalyst was reported to achieve a CO conversion of more than 80% and a CO selectivity of around 96% at low temperature.¹⁹ Kotobuki and co-workers synthesized Pt-Fe alloy nanoparticles on a mordenite support, which reached its maximum activity (around 70% CO conversion) at 150 °C with a CO selectivity of 75%.²³ Komatsu et al.²⁴ prepared Pt-Cu bimetallic nanoparticles on alumina with a liquid-phase reductive deposition method and found that this bimetallic catalyst was more active than Pt/SiO₂ in CO PROX. The Pt-Cu was reported to give in excess of 80% CO conversion at around 100 °C and reach its maximum CO conversion at around 150 °C with a CO selectivity of 50%. Xia's group²⁵ synthesized Pt-Pd alloy nanocages with hollow interiors and porous walls, which exhibited enhanced catalytic performance for CO PROX, with a maximum CO conversion of 95% at around 160 °C and a 100% CO selectivity at low temperature (below 100 °C). Mechanistic investigations suggest CO oxidation on Pt-M follows the altered dual-site L-H mechanism, which differentiates it from that on pure Pt. The improved selectivity was attributed to suppressed H₂ oxidation reaction between H₂ and adsorbed oxygen, which followed the Eley–Rideal (E-R) mechanism. However, most reported Pt-M catalysts can only achieve a high CO PROX selectivity in the ambient temperature range, with a rapid decrease in the selectivity when the temperature is raised. Because the CO PROX reaction typically requires an operating temperature window from around room temperature to 180 °C for practical applications,²² it is thus of high significance to find new Pt-M catalysts with both good activity and selectivity in this broadened temperature range.

In this work, we report a computation-aided methodology to guide the rational search of Pt-M catalysts for CO PROX and demonstrate the effectiveness of this method by selecting Pt-M following the DFT results and synthesizing the catalysts and testing the properties. The activity energy barriers for CO oxidation ($E_{A,COOR}$) and H₂ oxidation ($E_{A,HOR}$) are calculated and correlated with the d band center parameter (ϵ_d) of Pt-M. $E_{A,COOR}$ and the energy barrier difference ($\Delta E_A = E_{A,HOR} - E_{A,COOR}$) are identified as descriptors of the CO oxidation kinetics and PROX selectivity properties, with a compromising relationship between the two properties being discovered. Pt-Ni and Pt-Mn nanoparticle catalysts have been synthesized and tested, which testify to our theoretical model and demonstrate the ability to control CO PROX activity and selectivity properties in a broad temperature range by engineering the Pt-M active sites.

2. EXPERIMENTAL SECTION

2.1. Materials. Platinum acetylacetonate (Pt(acac)₂, 97%), nickel acetylacetonate (Ni(acac)₂, 95%), manganese carbonyl (Mn₂(CO)₁₀, 98%), alumina (Al₂O₃), oleylamine (OAm, technical grade 70%), oleic acid (OLA, technical grade 90%),

1,2-hexadecanediol (HDD, 90%, technical grade), and diphenyl ether (DPE, 99%, ReagentPlus) were purchased from Sigma-Aldrich. Toluene (C₇H₈, 99.9%) and anhydrous ethanol (EtOH, 95.3%) were purchased from Fisher Scientific. Carbon monoxide (CO, 5% balanced Ar), oxygen (O₂, 5% balanced Ar), hydrogen (H₂, 99.9999%), and argon (Ar, 99.9999%) gases were from Praxair.

2.2. Computational Details. The Cambridge Serial Total Energy Package (CASTEP) was used to perform the DFT calculations.²⁶ The 3D periodic-slab approach was used for representation of the infinite Pt alloy surface and interactions between this surface and isolated CO and H₂ molecules. The exchange and correlation energies were calculated using the generalized gradient approximation (GGA) and the Perdew–Burke–Ernzerhof (PBE) functional with ultrasoft pseudopotentials.²⁷ The bulk lattice of the Pt alloy was optimized before cleaving the surface. The Pt alloy surface was modeled by a $p(2 \times 2)$ unit cell with four layers of close-packed metal (111) surfaces with a vacuum layer of 18 Å. A plane wave basis set was used with a cutoff energy of 400 eV and a Monkhorst–Pack $5 \times 5 \times 1$ k -point mesh, and the thermal smearing was set at 0.1 eV. The bottom two layers of metal atoms were held fixed in their bulk positions, while the top two layers of atoms and all adsorbate degrees of freedom were allowed to relax. For simplicity, both CO and O were absorbed on the fcc top sites in this work. The adsorption energy (E_{ads}) was calculated as $E_{ads} = E_{total} - E_{slab} - E_{adsorbate}$, which is the energy gain with respect to the adsorbate in the gas phase and the metal slab at infinite separation. E_{total} is the total energy of the relaxed adsorbate–substrate system, E_{slab} is the energy of the slab with a clean surface, and $E_{adsorbate}$ is the energy of adsorbate in the gas phase. The d band center was defined as the average energy of the occupied d band relative to the Fermi level and calculated to be $\epsilon_d = \int_{-\infty}^0 E \rho_d(E) dE / \int_{-\infty}^0 \rho_d(E) dE$, where $\rho_d(E)$ is the projected d band density of states.

Transition states (TSs) were searched using a Complete LST/QST method.²⁸ In this approach, the search began by performing a linear synchronous transit (LST) maximization, which brackets the maximum between reactants and products, followed by an energy minimization in directions conjugate to the reaction pathway. The TS approximation obtained in this way was then used to perform a quadratic synchronous transit (QST) maximization. The above process was repeated until a stationary point was located.

2.3. Preparation of Catalysts. In this work, Pt-Mn, Pt-Ni, and Pt nanoparticles were first synthesized with wet chemistry methods. All of the synthetic experiments were conducted under continuous magnetic stirring and an argon atmosphere using a standard Schlenk line technique. Pt-Mn nanoparticles were prepared following a procedure reported in the literature,²⁹ which can be briefly described as follows. Pt(acac)₂ was first dissolved in DPE in the presence of OAm and OA. Then a Mn₂(CO)₁₀ stock solution was injected when the solution temperature reached 160 °C. This was followed by a rapid heating of the solution to 200 °C, at which the solution was kept for 30 min. To synthesize Pt-Ni nanoparticles, we dissolved both the metal precursors (Pt(acac)₂ and Ni(acac)₂) and HDD in DPE, OAm, and OA. Then the solution was heated to 230 °C and kept at that temperature for 1 h. Pt nanoparticles were synthesized by the same procedure except using Pt(acac)₂ as the metal precursor.

To prepare Pt-Mn/Al₂O₃, Pt-Ni/Al₂O₃, and Pt/Al₂O₃ nanoparticle catalysts, the as-synthesized Pt-Mn, Pt-Ni, and Pt

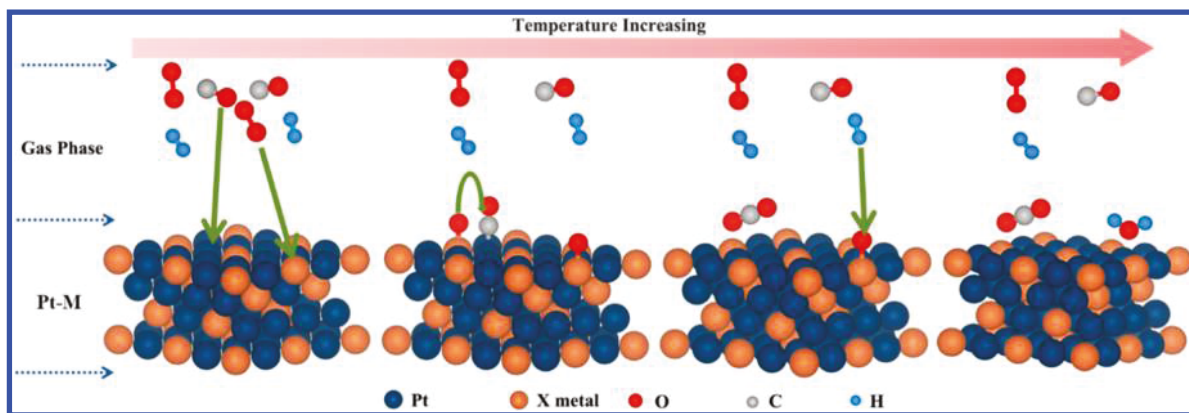


Figure 1. Schematic illustration of CO PROX pathways on Pt-M alloy catalyst.

nanoparticles were washed using ethanol for removal of excess amount of organic chemicals and redispersed in toluene. The designated amount of Al_2O_3 support material was added to the particle dispersion solution and the mixture stirred overnight. The products were collected and washed by centrifugation, followed by thermal treatment at $300\text{ }^\circ\text{C}$ for 1 h in air and 1 h in H_2 to generate a clean particle surface. Please see the [Supporting Information](#) for more experimental details.

2.4. Characterization of Catalysts. The as-prepared catalysts were characterized by taking transmission electron microscopy (TEM) images using a JEOL JEM-1230 microscope with an accelerating voltage of 120 kV. High-resolution transmission electron microscopy (HRTEM) was carried out by using a Tecnai TF 30 ST instrument with an accelerating voltage of 300 kV and a Schottky field-emission electron (FEG) gun as the electron source. X-ray diffraction (XRD) patterns were obtained on a Rigaku Ultima IV instrument with $\text{Cu K}\alpha$ radiation ($\lambda = 1.54056\text{ \AA}$). Metal loadings and compositions of the catalysts were determined using both quantitative energy dispersive X-ray (EDX) spectroscopy equipped on a JEOL-7401 field emission scanning electron microscope (FESEM) with an operating voltage at 25 kV and inductively coupled plasma-optical emission spectrometry (ICP-OES, 710 ICP-emission spectrometer, Agilent Technologies, Santa Clara, CA, USA). The oxidation state and binding energy of Pt-Mn, Pt-Ni, and Pt nanoparticles were characterized using X-ray photoelectron spectroscopy (XPS) on a VersaProbe II Scanning XPS Microprobe from Physical Electronics (PHI) under ultrahigh-vacuum condition. A monochromatic ($\text{Al K}\alpha$) X-ray beam ($E = 1486\text{ eV}$) was used to collect each spectrum.

2.5. Measurement of Catalytic Properties. The catalysts were first tested in the absence of H_2 to evaluate the catalytic properties in the CO oxidation reaction (COOR). The catalyst testing was conducted in a quartz tubular packed-bed reactor (PBR) with a diameter of 5 mm. The calcined catalyst powders were first pressed and crushed and then sieved to $250\text{--}500\text{ }\mu\text{m}$ pellet particles in size. Catalyst pellets (50 mg) were transferred into the PBR. A total volumetric flow rate of 100 sccm, which consisted of 1% CO , 1% O_2 , and 98% Ar as balance, was used. Prior to the CO oxidation test, the catalysts were reduced at $300\text{ }^\circ\text{C}$ for 1 h in 20% $\text{H}_2/80\%$ Ar to generate a clean catalyst surface. The product effluents were analyzed by one online gas chromatograph (Shimadzu GC-2014) equipped with one TCD detector. The CO PROX properties of the prepared catalysts were tested using a similar procedure with the entrance flow consisting of 1% CO , 0.5% O_2 , 70% H_2 , and 28.5% Ar as balance.

The CO conversion (X_{CO}), O_2 conversion (X_{O_2}), selectivity of CO_2 (S_{CO_2}), and CO oxidation rate values were determined using the equations

$$X_{\text{CO}} = \frac{C_{\text{CO}_2}}{C_{\text{CO}} + C_{\text{CO}_2}} \times 100\% \quad (1)$$

$$X_{\text{O}_2} = \frac{0.5C_{\text{CO}_2}}{C_{\text{O}_2} + 0.5C_{\text{CO}_2}} \times 100\% \quad (2)$$

$$S_{\text{CO}_2} = \frac{C_{\text{CO}_2}}{2(C_{\text{O}_2,0} - C_{\text{O}_2})} \times 100\% \quad (3)$$

$$\begin{aligned} -r_{\text{CO}'} &= \frac{F_{\text{CO},0}X_{\text{CO}}}{\Delta W_{\text{cat}}} = \frac{C_{\text{CO},0}v_0X_{\text{CO}}}{\Delta W_{\text{cat}}} = \frac{P}{RT}y_{\text{CO},0}\frac{v_0}{\Delta W_{\text{cat}}}X_{\text{CO}} \\ &= \frac{P}{RT}\frac{C_{\text{CO},0}}{C_T}\frac{v_0}{\Delta W_{\text{cat}}}\frac{C_{\text{CO}_2}}{C_{\text{CO},0}} = \frac{P}{RT}\frac{v_0}{\Delta W_{\text{cat}}}y_{\text{CO}_2} \end{aligned} \quad (4)$$

where C_{CO_2} , C_{CO} , and C_{O_2} are concentrations of CO_2 , CO , and O_2 in gas products, respectively, $C_{\text{O}_2,0}$ and $C_{\text{CO},0}$ are initial concentrations of O_2 and CO , respectively, $F_{\text{CO},0}$ is the entrance molar flow rate of CO , ΔW_{cat} is the amount of catalyst, v_0 is the entrance volumetric flow rate, y_{CO_2} is the mole fraction of CO_2 in the products and the reaction rate $-r_{\text{CO}'}$ is the disappearance rate of CO per mass of catalyst ($\text{mol}/(\text{s g}_{\text{cat}})$). The disappearance rate of CO per unit area of Pt-M nanoparticles ($-r_{\text{CO}''}$) was calculated using the equation $-r_{\text{CO}''} = -r_{\text{CO}'}/S_{\text{PtM}}$, where S_{PtM} is the specific surface area of the Pt-M nanoparticle catalysts. The turnover frequency (TOF) for CO oxidation was calculated as³⁰

$$\text{TOF} = \frac{-r_{\text{CO}''}N_{\text{A}}}{S'} \quad (5)$$

where N_{A} is Avogadro's number and S' is the surface atom density of Pt-M nanoparticles.

According to the rate law and the Arrhenius equation, $\ln(-r_{\text{CO}'})$ has a linear relationship with $1/T$, with the slope value being $E_{\text{A,app}}/R$, where $E_{\text{A,app}}$ is the apparent activation energy and R is the Boltzmann constant. By plotting the Arrhenius plots with $\ln(-r_{\text{CO}'})$ and $1/T$, the apparent activation energy can be obtained on the basis of the slope value of the plot.

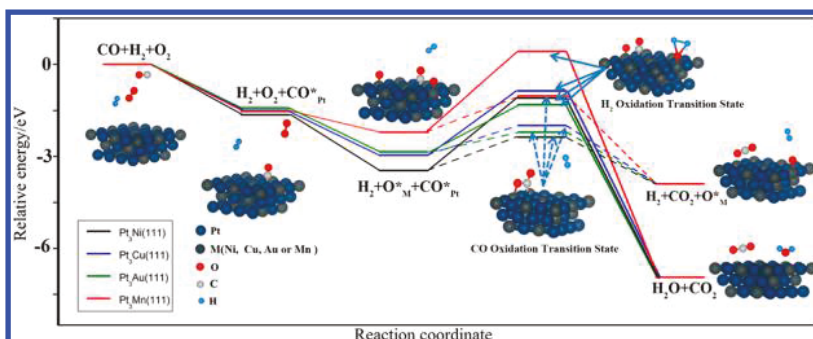


Figure 2. Energy diagram of CO PROX on Pt₃Ni, Pt₃Cu, Pt₃Au, and Pt₃Mn (111) surfaces. CO*_{Pt} and O*_M represent adsorbed CO at the Pt site and adsorbed oxygen at the M site, respectively.

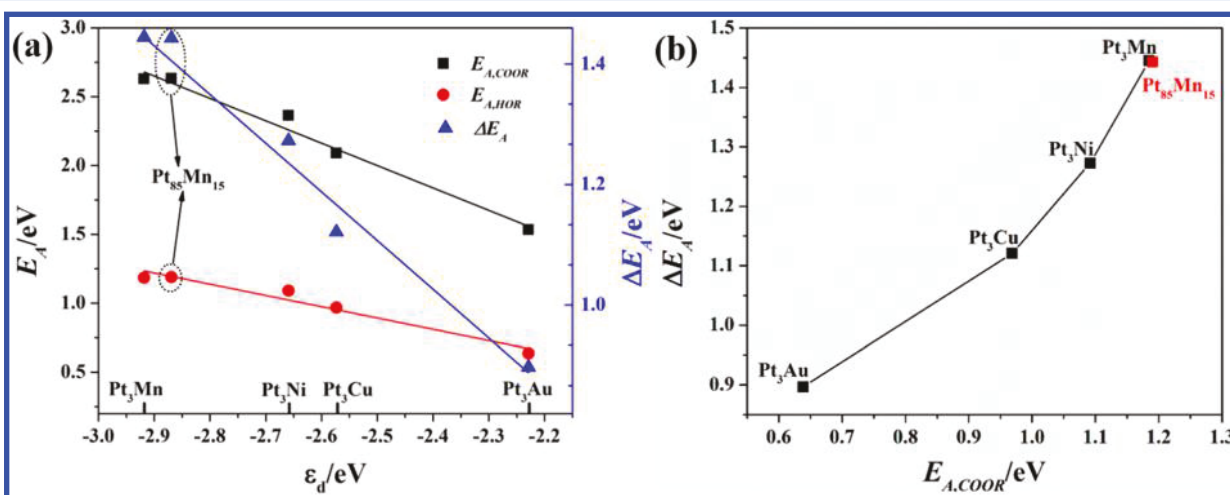


Figure 3. (a) $E_A - \epsilon_d$ and $\Delta E_A - \epsilon_d$ correlations for COOR and HOR and (b) ΔE_A as a function of $E_{A,COOR}$ on different Pt-M.

3. RESULTS AND DISCUSSION

On the basis of the current understanding,^{30–32} the CO PROX reaction mechanism on Pt-M catalyst can be illustrated in Figure 1 and depicted as follows: CO oxidation on Pt-M follows the dual-site L-H mechanism, with CO adsorption to the Pt site and O₂ dissociative adsorption to the M site. The adsorbed CO and oxygen atoms undergo surface reaction with each other, leading to CO₂ generation. This noncompetitive adsorption mechanism allows effective activation of O₂ at low temperature and thus dramatically improves the CO oxidation kinetics in comparison with that using Pt, on which O₂ cannot get effectively adsorbed at low temperature because of the competitive adsorption mechanism. H₂ undergoes competitive adsorption against CO at the Pt site and against oxygen at the M site. Previous studies found little adsorption of H₂ to Pt until around 90 °C when CO was present,¹⁴ which was attributed to a more negative CO adsorption energy. Because the M element, typically being less electronegative metals such as Fe, Co, and Sn,^{31,33} is precovered by oxygen, H₂ also cannot get effectively adsorbed. Thus, H₂ oxidation at low temperature has to undergo the E-L mechanism, in which gas-phase H₂ reacts with adsorbed oxygen at the M site. The reported high CO PROX selectivity on Pt-M catalysts, such as Pt-Sn, Pt-Fe, and Pt-Co,^{31,33} can be attributed to a relatively high $E_{A,HOR}$ that suppresses the H₂ oxidation at low temperature. The observed selectivity drop with reaction temperature on these catalysts can be related to an exponential increase in the rate constant of H₂ oxidation following the Arrhenius law.³¹

We conducted DFT simulations of the CO PROX pathways on several Pt-M systems, including Pt₃Ni, Pt₃Cu, Pt₃Au, and Pt₃Mn (111) surfaces, which were selected for their distinct electronic properties between different M elements.^{34–36} Figure 2 shows their DFT calculation favored energy diagrams, all of which followed the dual-site L-H mechanism and were in good agreement with previous mechanistic studies.^{32,37–39} The surface reaction between adsorbed CO at the Pt site (CO*_{Pt}) and atomic oxygen at the M site (O*_M) and the reaction between gas-phase H₂ molecules and O*_M were identified as the rate-limiting steps for the CO oxidation reaction (COOR) and H₂ oxidation reaction (HOR), respectively. Their corresponding energy barrier values were defined as $E_{A,COOR}$ and $E_{A,HOR}$, with the calculated values being summarized in Table S1. The Pt-M systems exhibited significantly different $E_{A,COOR}$ and $E_{A,HOR}$ values, indicating an apparent dependence of the Pt-M composition.

Previous theoretical studies have discovered the adsorption energy of molecules to a transition metal is largely determined by its d band center (ϵ_d), with one linear correlation often being observed.^{40–43} Considering that the activation energy barrier is the adsorption energy difference between an initial state and the affiliated transition state, it would also be correlated to ϵ_d . Figure 3a shows the plots of $E_{A,COOR}$, $E_{A,HOR}$, and ΔE_A (the energy difference between $E_{A,COOR}$ and $E_{A,HOR}$, i.e., $\Delta E_A = E_{A,HOR} - E_{A,COOR}$) against ϵ_d of the Pt-M. It was found that $E_{A,COOR}$, $E_{A,HOR}$, and ΔE_A all showed a good linear correlation with ϵ_d , suggesting the effectiveness of using ϵ_d as a catalyst parameter for describing the energy barriers. The

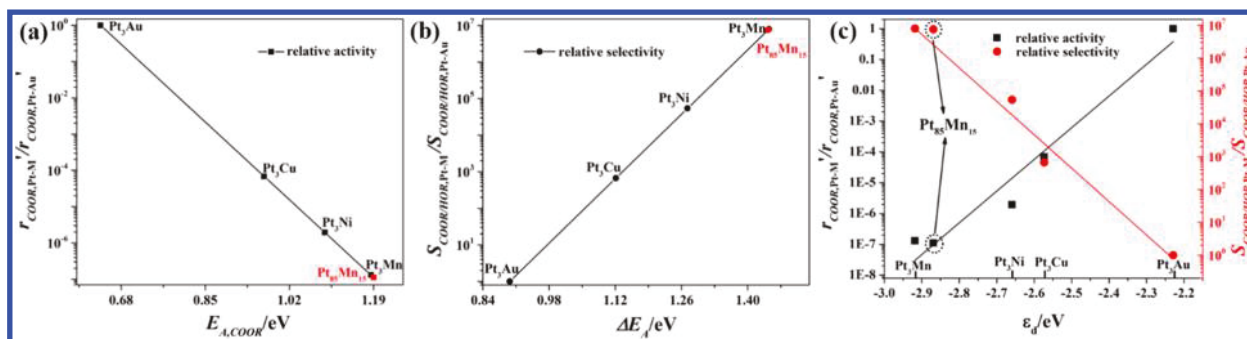


Figure 4. (a) Relative CO oxidation activity plot as a function of $E_{\text{A,COOR}}$. (b) Relative CO PROX selectivity plot as a function of ΔE_{A} . (c) Relative CO oxidation activity and PROX selectivity plots as a function of ϵ_{d} .

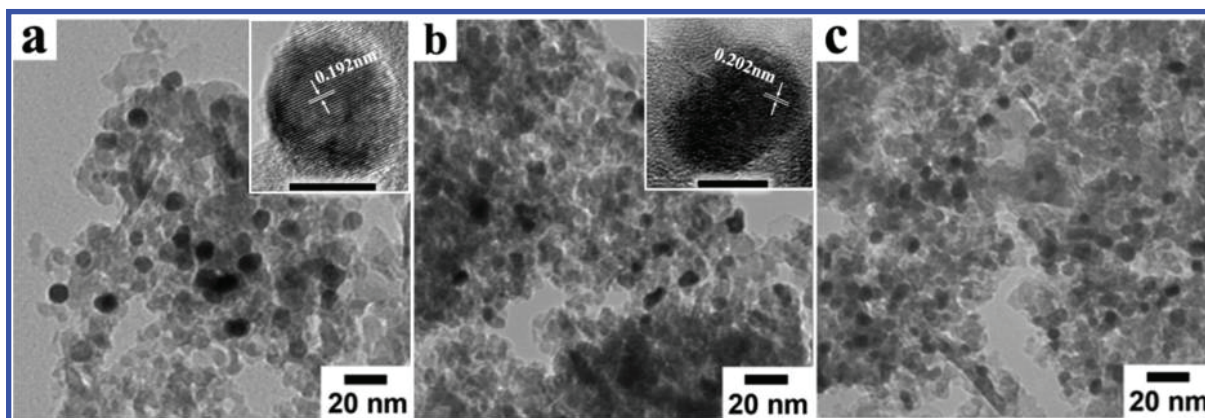


Figure 5. TEM of as-synthesized (a) Pt-Mn/Al₂O₃, (b) Pt-Ni/Al₂O₃, and (c) Pt/Al₂O₃ nanoparticle catalysts. The insets show HRTEM images of individual nanoparticles at a higher magnification. The scale bar is 5 nm in (a) and 10 nm in (b).

tenability of the ϵ_{d} parameter indicated the possibility to control the CO oxidation and PROX properties via engineering the Pt-M composition. Interestingly, ΔE_{A} exhibited a scaling relationship with $E_{\text{A,COOR}}$ (Figure 3b).

It is known that the overall rate of one reaction is largely determined by the rate constant of its limiting step and the rate constant is a function of its energy barrier following the Arrhenius law. Thus, $E_{\text{A,COOR}}$ can be used to describe the CO oxidation kinetics on Pt-M, i.e., $r_{\text{COOR}}' \propto \exp(-E_{\text{A,COOR}}/RT)$, where R is the gas constant and T is the reaction temperature. The energy barrier difference ΔE_{A} can be used to describe the CO PROX selectivity properties: i.e., $S_{\text{COOR/HOR}} = r_{\text{COOR}}'/r_{\text{HOR}}' \propto \exp(\Delta E_{\text{A}}/RT)$. Among the four studied Pt-M catalysts, Pt₃Au (111) exhibited the smallest $E_{\text{A,COOR}}$, suggesting the highest CO oxidation kinetics. To investigate the dependence of PROX properties on $E_{\text{A,COOR}}$ and ΔE_{A} , we set the CO oxidation activity and PROX selectivity on Pt-Au as a reference. The relative activity and selectivity using other Pt-M catalysts, considering that the pre-exponential factor in the Arrhenius equation typically remains the same order of magnitude using different Pt alloys,⁴⁴ can thus be described as

$$\begin{aligned} r_{\text{COOR,Pt-M}}'/r_{\text{COOR,Pt-Au}}' \\ \approx \exp[(E_{\text{A,COOR,Pt-Au}} - E_{\text{A,COOR,Pt-M}})/RT] \end{aligned} \quad (6)$$

$$\begin{aligned} S_{\text{COOR/HOR,Pt-M}}/S_{\text{COOR/HOR,Pt-Au}} \\ \approx \exp[(\Delta E_{\text{A,Pt-M}} - \Delta E_{\text{A,Pt-Au}})/RT] \end{aligned} \quad (7)$$

Figure 4a shows the correlation between the calculated relative activity and $E_{\text{A,COOR}}$ using different Pt-M at 400 K, an

average CO PROX operating temperature using Pt alloy catalysts.²² The relative COOR activity largely depended on $E_{\text{A,COOR}}$ and followed an exponential correlation. The four Pt-M systems under investigation exhibited different activities, following the sequence Pt-Au > Pt-Cu > Pt-Ni > Pt-Mn. Figure 4b shows the plot between the calculated relative selectivity and ΔE_{A} . It also exhibited an exponential correlation, with the sequence Pt-Au < Pt-Cu < Pt-Ni < Pt-Mn being observed. Figure 4c shows the plot of relative activity and relative selectivity against ϵ_{d} , both exhibiting a good exponential correlation. Considering the observed scaling relationship between ΔE_{A} and $E_{\text{A,COOR}}$ and their linear correlations with ϵ_{d} , the relative CO PROX activity and selectivity properties seemed to follow a compromising relationship. In another word, improvement of one property would be compensated by some decrease in the other property. Among the four Pt-M catalyst systems for CO PROX, Pt-Au was the most active but the least selective, corresponding to the least negative ϵ_{d} , and Pt-Mn was the least active but the most selective, corresponding to the most negative ϵ_{d} .

To validate the DFT calculations and the deduced Pt-M catalyst parameter-PROX property correlations, Pt-Mn/Al₂O₃ and Pt-Ni/Al₂O₃ nanoparticle catalysts were synthesized and tested, with Pt/Al₂O₃ being also tested for comparison. TEM characterizations of the three catalysts prepared showed good dispersion of metal nanoparticles on the support materials (Figure 5). Statistical analyses determined average particle sizes of 8.3 ± 2.3 nm for Pt-Mn/Al₂O₃, 5.8 ± 0.7 nm for Pt-Ni/Al₂O₃, and 6.2 ± 1.1 nm for Pt/Al₂O₃, respectively (Figure S1). The metal phases of the three catalysts were indexed to a face-centered cubic (fcc) structure from the powder X-ray

diffraction (PXRD) characterizations (Figure S2). The diffraction peaks of the Pt-Ni nanoparticles were positioned between those of pure Pt and Ni, indicating an alloy formation. No significant peak shifts were observed for the Pt-Mn nanoparticles, which could be due to similar sizes of Pt and Mn atoms and thus little influence of their alloying on the lattice parameter.^{45–47} The formation of Pt-Mn and Pt-Ni alloys were also characterized using high-resolution TEM (HRTEM) (insets of Figure 5). The Pt-Mn nanoparticles showed clear lattice fringes, indicating their crystalline characteristics. The lattice spacing was measured to be 0.192 nm, which was close to the data reported in the literature and was slightly smaller than 0.196 nm of Pt (100) planes.^{48,49} The lattice fringes of the Pt-Ni nanoparticles were spaced by 0.202 nm and were indexed to the (111) planes.⁵⁰ This value was significantly smaller than that of Pt (111) planes (0.227 nm). The differences in the measured lattice spacing of the Pt-Mn and Pt-Ni nanoparticles from that of Pt were consistent with the XRD characterizations and further confirmed their alloy formation. The Pt-Mn and Pt-Ni samples were also characterized using XPS (Figure S4). For both nanoparticles, Pt 4f_{7/2} peaks were used to analyze the chemical state of Pt because the Pt 4f_{5/2} signals were overlapped by that of Al 2p of Al₂O₃ (Figure S4a,c).⁵¹ The Pt-Ni sample exhibited the Pt 4f_{7/2} peak at around 71.02 eV (Figure S4a), consistent with its metallic state. This value represented about a 0.4 eV negative shift in the peak position in comparison with that of reference Pt (71.39 eV), indicating electron transfer between Pt and Ni when they were alloyed.⁵² The Ni 2p_{3/2} signals were deconvoluted into three peaks at 852.9, 853.8, and 857.3 eV and were ascribed to Ni⁰, NiO, and NiOOH, respectively. The XPS data matched with those of Pt-Ni alloys in previous studies,⁵² with the formation of surface Ni oxides being attributed to an exposure to the oxidative atmosphere. For Pt-Mn, the Pt 4f_{7/2} peak showed an even more negative shift to around 71 eV (Figure S4c), indicative of significant electron transfer from Mn to Pt. Two main peaks with binding energies of 642.2 and 653.6 eV were observed for Mn, which could be ascribed to Mn⁰ and Mn²⁺ species, as suggested by the literature data of Pt-Mn alloys.⁵³ The catalyst metal loadings were determined using EDX quantitative measurements and ICP-OES (Figure S3 and Table S2). The three catalysts had similar metal loadings, ranging from around 5 to 6.5 wt %.

The three catalysts were first tested in CO oxidation reactions. Figure 6a shows the CO conversion (X_{CO}) as a function of reaction temperature. Pt-Ni/Al₂O₃ was active even at room temperature, in agreement with literature studies.^{32,54} In comparison, Pt-Mn/Al₂O₃ and Pt/Al₂O₃ were not active until above around 100 °C. The significantly lower onset reaction temperature of Pt-Ni/Al₂O₃ suggested its higher activity in comparison to the other two catalysts in CO oxidation. Turnover frequency (TOF) values, which represent the intrinsic activity properties, were calculated for quantitative comparison of their activity (Figure 6b). The obtained trend of $TOF_{Pt-Ni} \gg TOF_{Pt-Mn} > TOF_{Pt}$ was in good agreement with the conversion profiles. The Arrhenius plots are presented in Figure 6c, with the slopes being used to calculate the apparent activation energy ($E_{A,app}$). The $E_{A,app}$ values were determined to be 29.2 kJ/mol using Pt-Ni/Al₂O₃, 39.0 kJ/mol using Pt-Mn/Al₂O₃, and 44.9 kJ/mol using Pt/Al₂O₃. Both Pt-Ni and Pt-Mn showed decreased $E_{A,app}$ in comparison to Pt, which was attributed to their altered dual-site L-H mechanism. Between the two alloy catalysts, the $E_{A,app}$ value of Pt-Ni was significantly

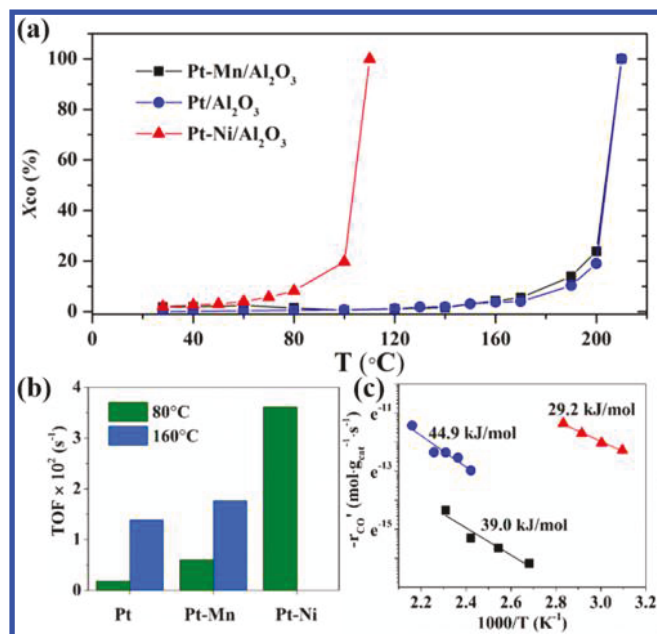


Figure 6. (a) CO conversion profile, (b) TOF, and (c) Arrhenius plots using the Pt-Mn/Al₂O₃, Pt-Ni/Al₂O₃, and Pt/Al₂O₃ catalysts under CO oxidation reaction conditions.

smaller than that of Pt-Mn. It suggested more promoted CO oxidation kinetics on Pt-Ni than on Pt-Mn, which was in good agreement with the DFT calculations.

The CO PROX properties of the Pt-Mn, Pt-Ni, and Pt catalysts are shown in Figure 7. In alignment with the CO oxidation testing results, Pt-Ni was the most active among the three catalysts. It exhibited 100% PROX selectivity at around room temperature, which rapidly dropped when the temperature was raised to above 50 °C. In the meantime the CO conversion increased from around 2.1% to 3%. In comparison, Pt-Mn showed a significantly lower activity and improved selectivity properties (Figure 7a,b), with 100% PROX selectivity remaining until about 170 °C. The Pt was the least active and selective among the three catalysts, demonstrating the advantages of the Pt-M catalytic structure in CO PROX. Figure 7c shows the determined TOF using the catalysts at 130 and 140 °C in CO PROX, with the trend remaining the same as in CO oxidation. The measured $E_{A,app}$ from the Arrhenius plots followed Pt-Ni < Pt-Mn < Pt (Figure 7d), which was the same as in the absence of H₂. These findings suggest that the CO oxidation still follows the dual-site L-H mechanism under the PROX conditions. The experimentally observed difference in the CO PROX properties between Pt-Ni and the Pt-Mn matched decently with the DFT simulations and thus further validated the theoretical model. It should be noted that the catalytic properties of the synthesized Pt-M alloy catalysts in this work may not be the best in comparison with some previous studies since the structure and morphology of the Pt-M alloy may have significant effects on the catalytic performance. For instance, Bao's group applied the interface confinement effect⁵⁵ and synthesized a highly active Pt-Ni structure containing both surface Ni oxides and subsurface Ni atoms, which exhibit very good activity in CO oxidation with carbon black (CB) as support.³⁵ The best activity for the Pt-Ni/CB catalysts was found to be 100% CO conversion at 320 K (47 °C). It is expected that the synergetic catalytic mechanism

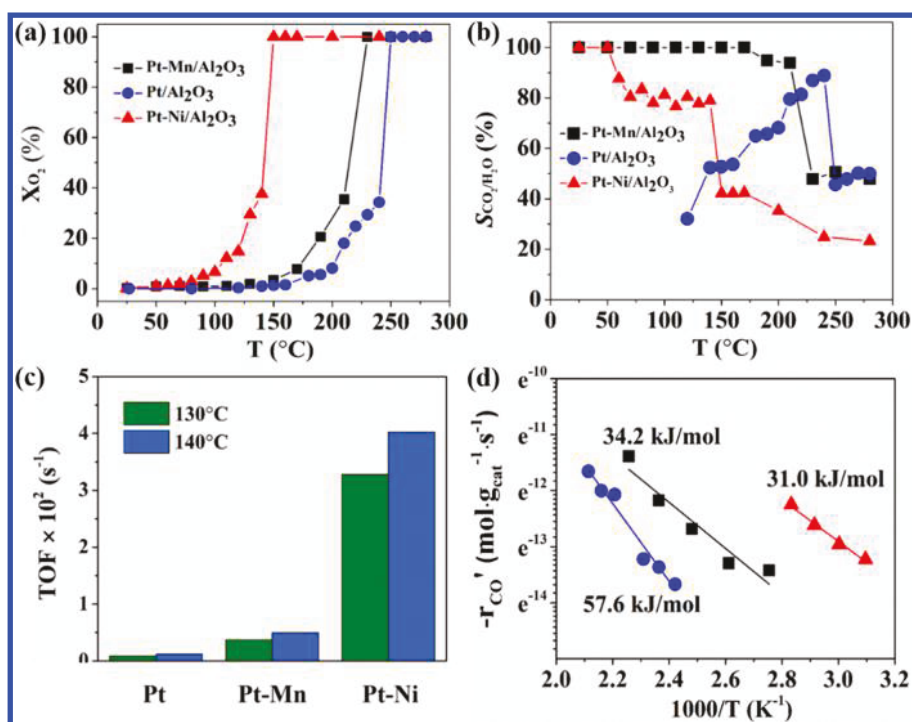


Figure 7. (a) O₂ conversion profile, (b) CO PROX selectivity, (c) TOF, and (d) Arrhenius plots using the Pt-Mn/Al₂O₃, Pt-Ni/Al₂O₃, and Pt/Al₂O₃ catalysts under CO PROX reaction conditions.

may be widely applied in other Pt-M bimetallic catalytic systems by manipulating the surface architecture.

In situ Fourier transform infrared spectroscopy (FTIR) experiments were conducted to investigate interactions between reacting species and working catalysts and the product generation. Figure 8 shows the absorbance spectra of CO, CO₂, and H₂O collected at different temperatures under the CO PROX testing conditions. The peak at 2090 cm⁻¹ was attributed to linearly adsorbed CO on the catalyst surface.⁵⁶ The two bands at 2327 and 2362 cm⁻¹ could be assigned to generated CO₂ molecules.⁵⁷ The band at 1590 cm⁻¹ was assigned to the δ(H₂O) bending.⁵⁸ Among the three catalysts, Pt-Ni exhibited the lowest temperature at which CO₂ signals were detected, confirming its higher activity in comparison to Pt-Mn and Pt. Pt-Mn exhibited the highest temperature at which H₂O signals were detected, confirming its superior selectivity properties in comparison to Pt-Ni. These observations were in good agreement with the catalytic property testing results and further supported the DFT simulations.

As discussed from the DFT simulations, the different CO PROX properties between Pt-Ni and Pt-Mn can be attributed to their different catalyst parameters and subsequently the altered energy barriers for CO oxidation and H₂ oxidation reactions. Pt-Ni was more active than Pt-Mn in CO oxidation and can be attributed to $E_{A,COOR,Pt-Ni} < E_{A,COOR,Pt-Mn}$ as revealed from DFT simulations, which were confirmed by their experimentally determined $E_{A,app}$ values. The smaller $E_{A,COOR}$ value for Pt-Ni than for Pt-Mn was primarily caused by weaker adsorption of oxygen at the Ni site than at the Mn site, which was the result of a deeper ϵ_d at the Ni site. On the other hand, the weaker adsorption of oxygen at the Ni site than at the Mn site led to $E_{A,HOR,Pt-Ni} < E_{A,HOR,Pt-Mn}$ and consequently $\Delta E_{A,Pt-Ni} < \Delta E_{A,Pt-Mn}$, which eventually resulted in a higher activity of Pt-Ni in H₂ oxidation and lower CO PROX selectivity in comparison to Pt-Mn. The good agreements between the DFT

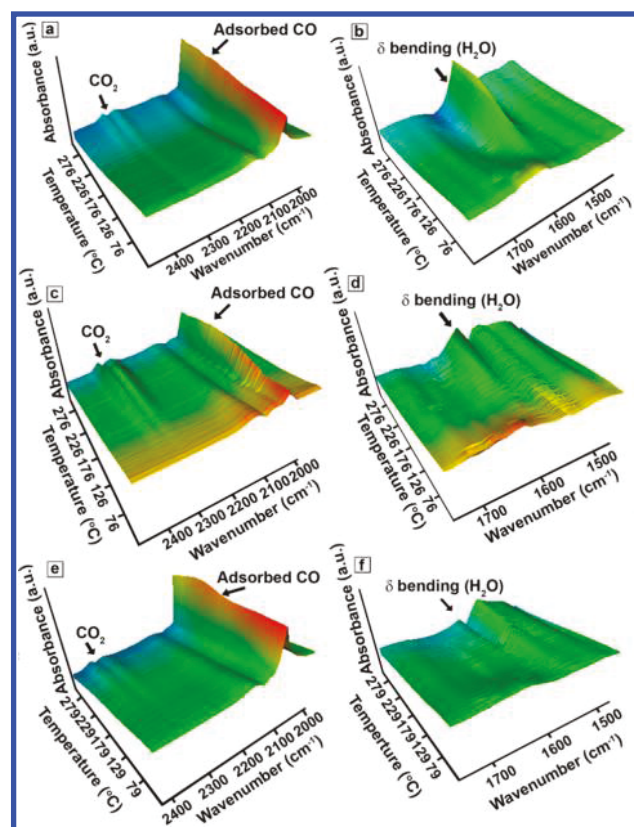


Figure 8. In situ FTIR spectra of produced CO₂ molecules, adsorbed CO, and produced H₂O (δ bending) using (a, b) Pt-Mn/Al₂O₃, (c, d) Pt-Ni/Al₂O₃, and (e, f) Pt/Al₂O₃ catalysts under the CO PROX reaction conditions.

predictions and the experimental results validated the use of $E_{A,COOR}$ and ΔE_A as descriptors of the CO PROX activity and

selectivity properties on Pt-M and their dependence on the catalyst parameters, as well as the discovered compromising relationship between the two properties. It should be noted that because the composition of the synthesized Pt-Mn was determined to be Pt₈₅Mn₁₅ by EDX and was not exactly the same as Pt₃Mn in the calculations, we also conducted DFT simulations on Pt₈₅Mn₁₅ to further validate our findings. The calculated data of $E_{A,COOR}$ and $E_{A,HOR}$ for Pt₈₅Mn₁₅ are summarized in Table S1, with the corresponding correlations being shown in Figures 3 and 4. Pt₈₅Mn₁₅ exhibited a trend similar to that for Pt₃Mn, indicating no dramatic change in the properties with a minor composition change. The simulation data using Pt₈₅Mn₁₅ agreed decently with the trend plots established using the Pt₃M model systems, which further validated the discovered compromising relationship between CO PROX activity and selectivity.

4. CONCLUSIONS

In summary, we conducted DFT simulations of CO PROX on model Pt-M catalyst systems, including Pt-Au, Pt-Cu, Pt-Ni, and Pt-Mn. The simulations determined the dual-site L-H mechanism for CO oxidation on Pt-M and the surface reaction between adsorbed CO at the Pt site and adsorbed oxygen at the M site as the rate-limiting step, with the corresponding $E_{A,COOR}$ being identified as the activity descriptor for this reaction. The simulations also determined the E-L mechanism for H₂ oxidation on Pt-M and identified $E_{A,HOR}$ for the reaction between H₂ and adsorbed oxygen as the activity descriptor, and they identified ΔE_A as the descriptor of the CO PROX selectivity properties. The $E_{A,COOR}$, $E_{A,HOR}$, and ΔE_A values were correlated to the Pt-M catalyst parameter ϵ_d . A compromising relationship between the CO PROX activity and selectivity properties was established.

Pt-Mn and Pt-Ni nanoparticle catalysts were prepared and experimentally tested to verify the DFT findings. Pt-Ni was found to be active in CO oxidation and highly selective in CO PROX at low temperature. However, the selectivity rapidly dropped when the temperature was above 50 °C. Pt-Mn was found to be less active than Pt-Ni in CO oxidation, with low activity in the low-temperature range. However, it exhibited 100% CO PROX selectivity until the temperature reached about 170 °C, which was significantly higher than the operating window of Pt-Ni. These experimental results confirmed the DFT simulations and validated the discovered compromising relationship between CO PROX activity and selectivity. These findings provide a rational Pt-M design strategy for developing new catalysts for CO PROX with engineering properties and operating temperature windows.

■ ASSOCIATED CONTENT

Supporting Information

The Supporting Information is available free of charge on the ACS Publications website at DOI: 10.1021/acscatal.8b00154.

Experimental details and characterization procedures and TEM, EDX, XRD, and XPS data (PDF)

■ AUTHOR INFORMATION

Corresponding Authors

*E-mail for J.Z.: zengj@ustc.edu.cn.

*E-mail for M.W.: mingzaiwu@gmail.com.

*E-mail for Z.P.: zpeng@uakron.edu.

ORCID

Jinlong Yang: 0000-0002-5651-5340

Jie Zeng: 0000-0002-8812-0298

Zhenmeng Peng: 0000-0003-1230-6800

Author Contributions

Y.P. and S.Y.H. contributed equally to this manuscript.

Notes

The authors declare no competing financial interest.

■ ACKNOWLEDGMENTS

We acknowledge the financial support of this work by National Science Foundation (CHE-1665265).

■ REFERENCES

- (1) Zhao, Z.; Lin, X.; Jin, R.; Dai, Y.; Wang, G. High Catalytic Activity in CO PROX Reaction of Low Cobalt-Oxide Loading Catalysts Supported on Nano-Particulate CeO₂-ZrO₂ Oxides. *Catal. Commun.* **2011**, *12*, 1448–1451.
- (2) Chen, G.; Yuan, Q.; Li, H.; Li, S. CO Selective Oxidation in a Microchannel Reactor for PEM Fuel Cell. *Chem. Eng. J.* **2004**, *101*, 101–106.
- (3) Laguna, O.; Sarria, F. R.; Centeno, M.; Odriozola, J. Gold Supported on Metal-Doped Ceria Catalysts (M= Zr, Zn and Fe) for the Preferential Oxidation of CO (PROX). *J. Catal.* **2010**, *276*, 360–370.
- (4) Fonseca, J. d. S. L.; Ferreira, H. S.; Bion, N.; Pirault-Roy, L.; do Carmo Rangel, M.; Duprez, D.; Epron, F. Cooperative Effect between Copper and Gold on Ceria for CO-PROX Reaction. *Catal. Today* **2012**, *180*, 34–41.
- (5) Jennings, J. R. *Catalytic Ammonia Synthesis: Fundamentals and Practice*; Springer Science & Business Media: New York, 2013; pp 8–17.
- (6) Kapteijn, F.; Singoredjo, L.; Andreini, A.; Moulijn, J. Activity and Selectivity of Pure Manganese Oxides in the Selective Catalytic Reduction of Nitric Oxide with Ammonia. *Appl. Catal. B* **1994**, *3*, 173–189.
- (7) Fu, Q.; Saltsburg, H.; Flytzani-Stephanopoulos, M. Active Nonmetallic Au and Pt Species on Ceria-Based Water-Gas Shift Catalysts. *Science* **2003**, *301*, 935–938.
- (8) Acres, G.; Frost, J.; Hards, G.; Potter, R.; Ralph, T.; Thompson, D.; Burstein, G.; Hutchings, G. Electrocatalysts for Fuel Cells. *Catal. Today* **1997**, *38*, 393–400.
- (9) Denkwitz, Y.; Schumacher, B.; Kučerová, G.; Behm, R. J. Activity, Stability, and Deactivation Behavior of Supported Au/TiO₂ Catalysts in the CO Oxidation and Preferential CO Oxidation Reaction at Elevated Temperatures. *J. Catal.* **2009**, *267*, 78–88.
- (10) Schubert, M.; Kahllich, M.; Gasteiger, H.; Behm, R. Correlation between CO Surface Coverage and Selectivity/Kinetics for the Preferential CO Oxidation over Pt/ γ -Al₂O₃ and Au/ α -Fe₂O₃: An In-situ DRIFTS Study. *J. Power Sources* **1999**, *84*, 175–182.
- (11) Widmann, D.; Behm, R. J. Active Oxygen on a Au/TiO₂ Catalyst: Formation, Stability, and CO Oxidation Activity. *Angew. Chem., Int. Ed.* **2011**, *50*, 10241–10245.
- (12) Oh, S. H.; Sinkevitch, R. M. Carbon Monoxide Removal from Hydrogen-rich Fuel Cell Feedstreams by Selective Catalytic Oxidation. *J. Catal.* **1993**, *142*, 254–262.
- (13) Kahllich, M.; Gasteiger, H.; Behm, R. Kinetics of the Selective CO Oxidation in H₂-rich Gas on Pt/Al₂O₃. *J. Catal.* **1997**, *171*, 93–105.
- (14) Wootsch, A.; Descorme, C.; Duprez, D. Preferential Oxidation of Carbon Monoxide in the Presence of Hydrogen (PROX) over Ceria-Zirconia and Alumina-Supported Pt Catalysts. *J. Catal.* **2004**, *225*, 259–266.
- (15) Shapovalov, V.; Metiu, H. Catalysis by Doped Oxides: CO Oxidation by Au_xCe_{1-x}O₂. *J. Catal.* **2007**, *245*, 205–214.
- (16) Qiao, B.; Wang, A.; Li, L.; Lin, Q.; Wei, H.; Liu, J.; Zhang, T. Ferric Oxide-Supported Pt Subnano Clusters for Preferential

Oxidation of CO in H₂-rich Gas at Room Temperature. *ACS Catal.* **2014**, *4*, 2113–2117.

(17) Huang, S.; Hara, K.; Fukuoka, A. Green Catalysis for Selective CO Oxidation in Hydrogen for Fuel Cell. *Energy Environ. Sci.* **2009**, *2*, 1060–1068.

(18) Korotkikh, O.; Farrauto, R. Selective Catalytic Oxidation of CO in H₂: Fuel Cell Applications. *Catal. Today* **2000**, *62*, 249–254.

(19) Ko, E. Y.; Park, E. D.; Lee, H. C.; Lee, D.; Kim, S. Supported Pt–Co Catalysts for Selective CO Oxidation in a Hydrogen-Rich Stream. *Angew. Chem., Int. Ed.* **2007**, *46*, 734–737.

(20) Uysal, G.; Akın, A. N.; Önsan, Z. İ.; Yıldırım, R. Preferential CO Oxidation over Pt–SnO₂/Al₂O₃ in Hydrogen Rich Streams Containing CO₂ and H₂O (CO Removal from H₂ with PROX). *Catal. Lett.* **2006**, *111*, 173–176.

(21) Lobera, M.; Téllez, C.; Herguido, J.; Menéndez, M. Catalytic Purification of H₂-rich Streams by CO-PROX over Pt–Co–Ce/γ-Al₂O₃ in Fluidized Bed Reactors. *Catal. Today* **2010**, *157*, 404–409.

(22) Liu, K.; Wang, A.; Zhang, T. Recent Advances in Preferential Oxidation of CO Reaction over Platinum Group Metal Catalysts. *ACS Catal.* **2012**, *2*, 1165–1178.

(23) Kotobuki, M.; Watanabe, A.; Uchida, H.; Yamashita, H.; Watanabe, M. Reaction Mechanism of Preferential Oxidation of Carbon Monoxide on Pt, Fe, and Pt–Fe/mordenite Catalysts. *J. Catal.* **2005**, *236*, 262–269.

(24) Komatsu, T.; Takasaki, M.; Ozawa, K.; Furukawa, S.; Muramatsu, A. PtCu Intermetallic Compound Supported on Alumina Active for Preferential Oxidation of CO in Hydrogen. *J. Phys. Chem. C* **2013**, *117*, 10483–10491.

(25) Zhang, H.; Jin, M.; Liu, H.; Wang, J.; Kim, M. J.; Yang, D.; Xie, Z.; Liu, J.; Xia, Y. Facile Synthesis of Pd–Pt Alloy Nanocages and Their Enhanced Performance for Preferential Oxidation of CO in Excess Hydrogen. *ACS Nano* **2011**, *5*, 8212–8222.

(26) Clark, S. J.; Segall, M. D.; Pickard, C. J.; Hasnip, P. J.; Probert, M. I.; Refson, K.; Payne, M. C. First Principles Methods Using CASTEP. *Z. Kristallogr. - Cryst. Mater.* **2005**, *220*, 567–570.

(27) Perdew, J. P.; Burke, K.; Ernzerhof, M. Generalized Gradient Approximation Made Simple. *Phys. Rev. Lett.* **1996**, *77*, 3865.

(28) Govind, N.; Petersen, M.; Fitzgerald, G.; King-Smith, D.; Andzelm, J. A Generalized Synchronous Transit Method for Transition State Location. *Comput. Mater. Sci.* **2003**, *28*, 250–258.

(29) Kang, Y.; Murray, C. B. Synthesis and Electrocatalytic Properties of Cubic Mn–Pt Nanocrystals (Nanocubes). *J. Am. Chem. Soc.* **2010**, *132*, 7568–7569.

(30) Hwang, S. Y.; Zhang, C.; Yurchekfrod, E.; Peng, Z. Property of Pt–Ag Alloy Nanoparticle Catalysts in Carbon Monoxide Oxidation. *J. Phys. Chem. C* **2014**, *118*, 28739–28745.

(31) Chorkendorff, I.; Niemantsverdriet, J. W. *Concepts of Modern Catalysis and Kinetics*. Wiley: Hoboken, NJ, 2017; pp 23–73.

(32) Hwang, S. Y.; Yurchekfrod, E.; Zhang, C.; Peng, Z. Low-Temperature Preferential Oxidation of Carbon Monoxide on Pt₃Ni Alloy Nanoparticle Catalyst with Engineered Surface. *ChemCatChem* **2016**, *8*, 97–101.

(33) Ko, E.-Y.; Park, E. D.; Seo, K. W.; Lee, H. C.; Lee, D.; Kim, S. A Comparative Study of Catalysts for the Preferential CO Oxidation in Excess Hydrogen. *Catal. Today* **2006**, *116*, 377–383.

(34) Kandoi, S.; Gokhale, A.; Grabow, L.; Dumesic, J.; Mavrikakis, M. Why Au and Cu Are More Selective Than Pt for Preferential Oxidation of CO at Low Temperature. *Catal. Lett.* **2004**, *93*, 93–100.

(35) Mu, R.; Fu, Q.; Xu, H.; Zhang, H.; Huang, Y.; Jiang, Z.; Zhang, S.; Tan, D.; Bao, X. Synergetic Effect of Surface and Subsurface Ni Species at Pt–Ni Bimetallic Catalysts for CO Oxidation. *J. Am. Chem. Soc.* **2011**, *133*, 1978–1986.

(36) Yu, W.; Porosoff, M. D.; Chen, J. G. Review of Pt-Based Bimetallic Catalysis: from Model Surfaces to Supported Catalysts. *Chem. Rev.* **2012**, *112*, 5780–5817.

(37) Gómez, L. E.; Sollier, B. M.; Mizrahi, M. D.; López, J. M. R.; Miró, E. E.; Boix, A. V. Preferential CO Oxidation on Pt–Cu/Al₂O₃ Catalysts with Low Pt Loadings. *Int. J. Hydrogen Energy* **2014**, *39*, 3719–3729.

(38) Zhou, S.; Jackson, G. S.; Eichhorn, B. AuPt Alloy Nanoparticles for CO-Tolerant Hydrogen Activation: Architectural Effects in Au–Pt Bimetallic Nanocatalysts. *Adv. Funct. Mater.* **2007**, *17*, 3099–3104.

(39) Ko, E.-Y.; Park, E. D.; Seo, K. W.; Lee, H. C.; Lee, D.; Kim, S. Selective CO Oxidation in the Presence of Hydrogen over Supported Pt Catalysts Promoted with Transition Metals. *Korean J. Chem. Eng.* **2006**, *23*, 182–187.

(40) Hammer, B.; Nørskov, J. Why Gold Is the Noblest of All the Metals. *Nature* **1995**, *376*, 238–240.

(41) Hammer, B.; Nørskov, J. Electronic Factors Determining the Reactivity of Metal Surfaces. *Surf. Sci.* **1995**, *343*, 211–220.

(42) Hammer, B.; Nørskov, J. K. Theoretical Surface Science and Catalysis—Calculations and Concepts. *Adv. Catal.* **2000**, *45*, 71–129.

(43) Shen, X.; Pan, Y.; Liu, B.; Yang, J.; Zeng, J.; Peng, Z. More Accurate Depiction of Adsorption Energy on Transition Metals Using Work Function as One Additional Descriptor. *Phys. Chem. Chem. Phys.* **2017**, *19*, 12628–12632.

(44) Lian, X.; Guo, W.; Liu, F.; Yang, Y.; Xiao, P.; Zhang, Y.; Tian, W. DFT Studies on Pt₃M (M = Pt, Ni, Mo, Ru, Pd, Rh) Clusters for CO Oxidation. *Comput. Mater. Sci.* **2015**, *96*, 237–245.

(45) Xu, C.; Tian, Z.; Shen, P.; Jiang, S. P. Oxide (CeO₂, NiO, Co₃O₄ and Mn₃O₄)-Promoted Pd/C Electrocatalysts for Alcohol Electro-oxidation in Alkaline Media. *Electrochim. Acta* **2008**, *53*, 2610–2618.

(46) Yang, X.; Wang, X.; Zhang, G.; Zheng, J.; Wang, T.; Liu, X.; Shu, C.; Jiang, L.; Wang, C. Enhanced Electrocatalytic Performance for Methanol Oxidation of Pt Nanoparticles on Mn₃O₄-Modified Multi-Walled Carbon Nanotubes. *Int. J. Hydrogen Energy* **2012**, *37*, 11167–11175.

(47) Thirupathi, B.; Smirniotis, P. G. Nickel-Doped Mn/TiO₂ as an Efficient Catalyst for the Low-Temperature SCR of NO with NH₃: Catalytic Evaluation and Characterizations. *J. Catal.* **2012**, *288*, 74–83.

(48) Shen, Y.; Xiao, K.; Xi, J.; Qiu, X. Comparison Study of Few-Layered Graphene Supported Platinum and Platinum Alloys for Methanol and Ethanol Electro-Oxidation. *J. Power Sources* **2015**, *278*, 235–244.

(49) Ammam, M.; Easton, E. B. Oxygen Reduction Activity of Binary PtMn/C, Ternary PtMnX/C (X = Fe, Co, Ni, Cu, Mo and Sn) and Quaternary PtMnCuX/C (X = Fe, Co, Ni, and Sn) and PtMnMoX/C (X = Fe, Co, Ni, Cu and Sn) Alloy Catalysts. *J. Power Sources* **2013**, *236*, 311–320.

(50) Zhou, Y.-Y.; Liu, C.-H.; Liu, J.; Cai, X.-L.; Lu, Y.; Zhang, H.; Sun, X.-H.; Wang, S.-D. Self-Decoration of PtNi Alloy Nanoparticles on Multiwalled Carbon Nanotubes for Highly Efficient Methanol Electro-Oxidation. *Nano-Micro Lett.* **2016**, *8*, 371–380.

(51) Yang, T.; Huo, Y.; Liu, Y.; Rui, Z.; Ji, H. Efficient Formaldehyde Oxidation over Nickel Hydroxide Promoted Pt/γ-Al₂O₃ with A Low Pt Content. *Appl. Catal. B* **2017**, *200*, 543–551.

(52) Wang, G. J.; Gao, Y. Z.; Wang, Z. B.; Du, C. Y.; Wang, J. J.; Yin, G. P. Investigation of PtNi/C Anode Electrocatalysts for Direct Borohydride Fuel Cell. *J. Power Sources* **2010**, *195*, 185–189.

(53) Ammam, M.; Prest, L. E.; Pauric, A. D.; Easton, E. B. Synthesis, Characterization and Catalytic Activity of Binary PtMn/C Alloy Catalysts towards Ethanol Oxidation. *J. Electrochem. Soc.* **2012**, *159*, B195–B200.

(54) Ko, E.-Y.; Park, E. D.; Seo, K. W.; Lee, H. C.; Lee, D.; Kim, S. Pt–Ni/γ-Al₂O₃ Catalyst for the Preferential CO Oxidation in the Hydrogen Stream. *Catal. Lett.* **2006**, *110*, 275–279.

(55) Fu, Q.; Li, W.-X.; Yao, Y.; Liu, H.; Su, H.-Y.; Ma, D.; Gu, X.-K.; Chen, L.; Wang, Z.; Zhang, H. Interface-Confined Ferrous Centers for Catalytic Oxidation. *Science* **2010**, *328*, 1141–1144.

(56) Pillonel, P.; Derrouiche, S.; Bourane, A.; Gaillard, F.; Vernoux, P.; Bianchi, D. Impact of the Support on the Heat of Adsorption of the Linear CO Species on Pt-Containing Catalysts. *Appl. Catal., A* **2005**, *278*, 223–231.

(57) Toda, Y.; Hirayama, H.; Kuganathan, N.; Torrisi, A.; Sushko, P. V.; Hosono, H. Activation and Splitting of Carbon Dioxide on the Surface of An Inorganic Electride Material. *Nat. Commun.* **2013**, *4*, 2378.

(58) Al-Abadleh, H. A.; Grassian, V. FT-IR Study of Water Adsorption on Aluminum Oxide Surfaces. *Langmuir* **2003**, *19*, 341–347.